MATERIALS SCIENCE

Wafer-patterned, permeable, and stretchable liquid metal microelectrodes for implantable bioelectronics with chronic biocompatibility

Qiuna Zhuang[1], Kuanming Yao[2], Mengge Wu[2], Zhuogui Lei[3], Fan Chen[1], Jiyu Li[2,4], Quanjing Mei[5], Yingying Zhou[5], Qiyao Huang[1], Xin Zhao[5], Ying Li[3], Xinge Yu[2,4]*, Zijian Zheng[1,6,7,8]*

Implantable bioelectronics provide unprecedented opportunities for real-time and continuous monitoring of physiological signals of living bodies. Most bioelectronics adopt thin-film substrates such as polyimide and polydimethylsiloxane that exhibit high levels of flexibility and stretchability. However, the low permeability and relatively high modulus of these thin films hamper the long-term biocompatibility. In contrast, devices fabricated on porous substrates show the advantages of high permeability but suffer from low patterning density. Here, we report a wafer-scale patternable strategy for the high-resolution fabrication of supersoft, stretchable, and permeable liquid metal microelectrodes (μLMEs). We demonstrate 2-μm patterning capability, or an ultrahigh density of ~75,500 electrodes/cm², of μLME arrays on a wafer-size (diameter, 100 mm) elastic fiber mat by photolithography. We implant the μLME array as a neural interface for high spatiotemporal mapping and intervention of electrocorticography signals of living rats. The implanted μLMEs have chronic biocompatibility over a period of eight months.

INTRODUCTION

Implantable and skin-attachable bioelectronics are essential in providing real-time and continuous monitoring of physiological signals for future point-of-care diagnostics (*1*–*4*), therapeutics (*5*, *6*), rehabilitation (*7*), and augmented reality (*8*). Over the past decades, scientists have made remarkable achievements in developing highly stretchable electronics by patterning devices and circuits on polymeric thin-film substrates such as polyethylene naphthalate, polyimide (PI), and elastomers [e.g., polydimethylsiloxane (PDMS), polystyrene-ethylene-butylene-styrene, and Ecoflex] (*9*–*12*). With proper structural and materials design, these stretchable devices can have not only electronic functions similar to or even superior to those fabricated on rigid substrates but also marked compliance that enables conformable contact with soft tissues avoiding interfacial delamination during movements (*13*–*15*).

In addition to a high stretchability, chronic (long-term) biocompatibility is of paramount importance to bioelectronics (*16*). It has been reported that chronic attachment of thin-film (e.g., PDMS) devices on skin and tissue surfaces may result in thermophysiological discomforts such as clamminess, dampness, skin inflammation (*17*, *18*), and even malignancies during chronic implantation (*19*) due to inadequate permeability and the smooth surface. When the polymeric substrate is too stiff (e.g., PI) in comparison to the soft tissues, chronic implantation may also lead to tissue scarring (*20*). Therefore, it is advocated very recently to develop supersoft and permeable types of stretchable electronics, where electronic devices are fabricated on porous elastomeric substrates that offer high stretchability and permeability to air, moisture, and even liquid (*21*, *22*). These porous elastomeric substrates are mainly fabricated either by engineering micropores on those polymeric thin films (*23*–*25*) or by direct electrospinning process (*26*–*29*). Notably, electrospinning displays advantages in the tunability of the porosity, elasticity, and thickness, and it has been widely applied for fabricating various biomedical devices (*30*, *31*).

On the planar substrates, there have been a large number of works to pattern stretchable electrodes (*32*–*41*), such as gold and liquid metal (*42*), with high resolutions. However, because of the large surface roughness and porosity, it has been extremely challenging to pattern microelectrodes in high resolution on those supersoft and permeable substrates. The patternable feature sizes demonstrated to date typically range from 100 μm to millimeters(*21*), which results in a low electrode density of 1 to 10 electrodes/cm². This is far from meeting the demand for advanced bioelectronics aiming for mapping and intervention with a high spatial and temporal resolution, which typically requires a patterning resolution down to a few micrometers (*13*), or an electrode density of over 100 electrodes/cm² (*43*–*47*).

In this work, we report wafer-scale patterning of permeable and stretchable liquid metal (LM) microelectrodes (μLMEs) on fibrous substrates with high resolutions down to 2 μm and an ultrahigh patterning density over 75,000 electrodes/cm² by photolithography. These μLMEs show tissue-like mechanical softness, outstanding electrical conductance when stretched up to 1000% strain, and chronic biocompatibility over chronic on-skin attachment and implantation testings. We demonstrate a supersoft and permeable

¹Laboratory for Advanced Interfacial Materials and Devices, School of Fashion and Textiles, The Hong Kong Polytechnic University, Hong Kong SAR, China. ²Department of Biomedical Engineering, City University of Hong Kong, Hong Kong SAR, China. ³Department of Neuroscience, City University of Hong Kong, Hong Kong SAR, China. ⁴Hong Kong Centre for Cerebro-Cardiovascular Health Engineering (COCHE), Hong Kong Science Park, Hong Kong SAR, China. ⁵Department of Biomedical Engineering, The Hong Kong Polytechnic University, Hong Kong SAR, China. ⁶Department of Applied Biology and Chemical Technology, The Hong Kong Polytechnic University, Hong Kong SAR, China. ⁷Research Institute for Intelligent Wearable Systems (RI-IWEAR), The Hong Kong Polytechnic University, Hong Kong SAR, China. ⁸Research Institute for Smart Energy (RISE), The Hong Kong Polytechnic University, Hong Kong SAR, China.
*Corresponding author. Email: tczzheng@polyu.edu.hk (Z.Z.); xingeyu@cityu.edu.hk (X.Y.)

neural interface for high–spatiotemporal-resolution mapping and intervention of electrocorticography (ECoG) signals.

RESULTS

Fabrication of permeable and μLMEs

Figure 1A shows a schematic illustration of the fabrication process of wafer-scale μLMEs, which consists of four main steps: (i) photolithography of Ag on a SiO$_2$ wafer premodified with a thin layer of water-soluble dextran; (ii) electrospinning of a fibrous poly(styrene-*block*-butadiene-*block*-styrene) (SBS) mat onto the Ag micropatterns; (iii) dissolving of the dextran layer and transfer of the Ag micropatterns from the SiO$_2$ wafer onto the SBS fiber mat; and (iv) selective wetting of LM on the Ag-cover areas to generate μLMEs.
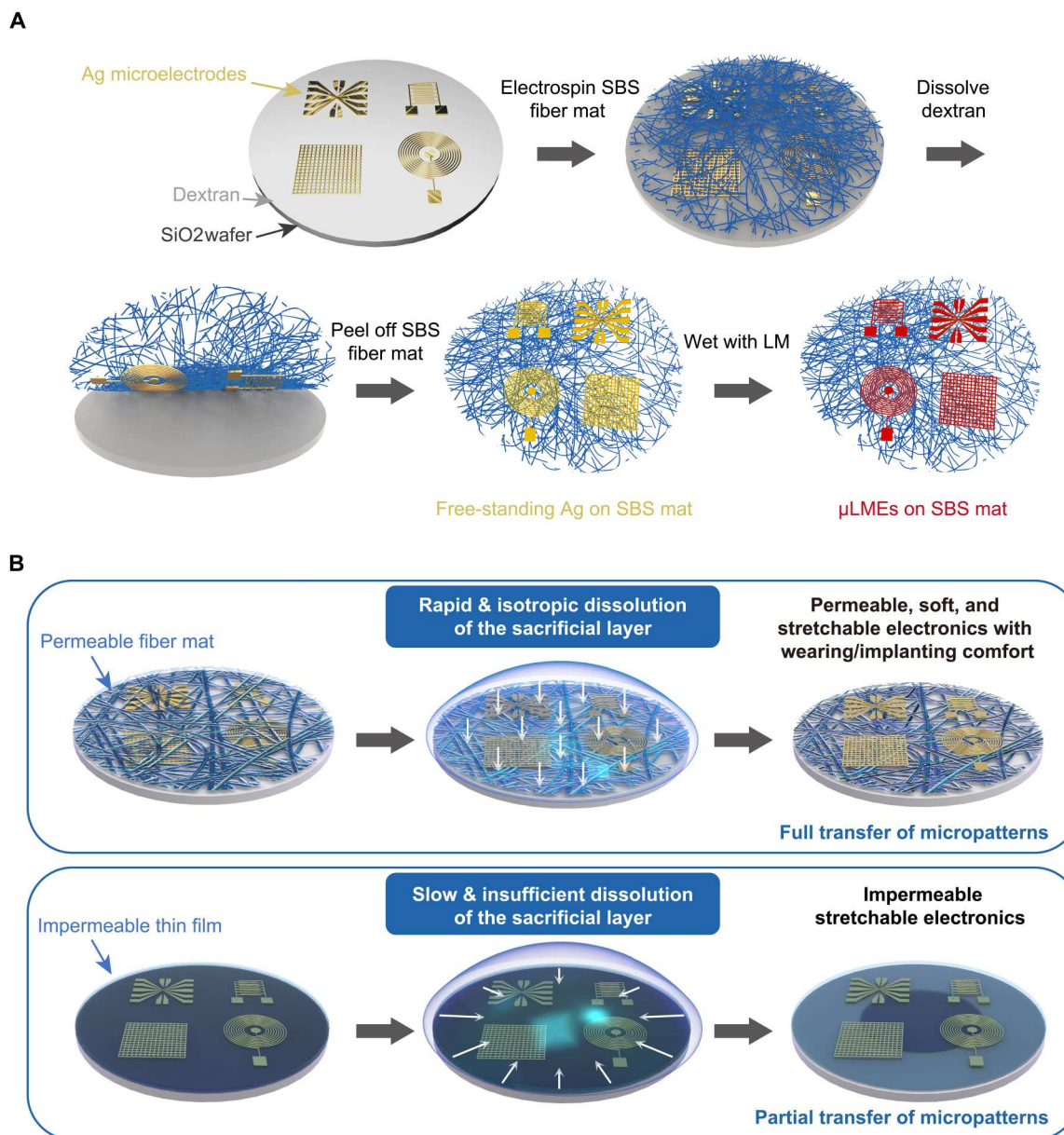
Fig. 1. Fabrication process of stretchable and permeable liquid metal microelectrodes (μLMEs). (**A**) Schematic illustration of the fabrication process of μLMEs, which consists of four main steps: (i) photolithography of Ag on a SiO$_2$ wafer premodified with a thin layer of water-soluble dextran, (ii) electrospinning of a fibrous SBS mat onto the Ag micropatterns, (iii) dissolving of the dextran layer and transfer of the Ag micropatterns from the SiO$_2$ wafer onto the SBS fiber mat, and (iv) selective wetting of LM on the Ag-covered areas to generate μLMEs. (**B**) Schematic comparison of the different dissolution processes of the sacrificial layer by using permeable fiber mats or impermeable thin films. The use of permeable substrate significantly improves the contact area between the sacrificial layer and the solvent because the solvent can easily penetrate the porous fiber network. Therefore, the sacrificial layer can be fully dissolved in a short time in an isotropic manner, and the Ag micropatterns can be fully transferred. In contrast, the solvent can only contact the sacrificial layer from the edge of the substrate when using impermeable thin film substrates, e.g., PDMS, resulting in the slow and insufficient dissolution of the sacrificial layer and thus the partial transfer of the Ag micropatterns.

The direct electrospinning of the SBS fiber mat onto Ag micropatterns is the key step, and it addresses two critical challenges in the fabrication of microsized LM on porous and stretchable substrates (Fig. 1B). First of all, the direct electrospinning of SBS fibers ensures a conformal contact of the fibrous substrates with the Ag micropatterns. Therefore, when the dextran layer is dissolved by water, Ag micropatterns will adhere firmly to the SBS fiber mat and achieve a complete pattern transfer. Second, the fibrous structure of the receiving SBS substrate offers a rapid penetration of water and a large water/dextran contact interface, so as to achieve a fast and isotropic dissolution of dextran. Such an isotropic dissolution of the sacrificial layer is also critical to achieving a complete pattern transfer over a large area (fig. S1).

We chose eutectic gallium indium (EGaIn) alloy as the LM. EGaIn shows a low melting temperature of 15.4°C (48) and stable conductive properties even under large tensile strains (49–55) because of its intrinsic fluidity (56, 57) in comparison to those solid electrodes. In addition, the low modulus and high biocompatibility of EGaIn also benefit the applications in soft and stretchable bioelectronics (58–60).

As a proof of concept, we patterned 300-nm-thick Ag with feature sizes ranging from 2 to 1000 μm on a wafer substrate (diameter, 100 mm) (Fig. 2A, inset). The SiO_2 wafer surface was previously spin-coated with a 10-nm-thick dextran layer with a smooth surface (fig. S2). We then electrospun a 100-μm-thick SBS fiber mat on the wafer surface (fig. S3). After a plasma treatment on the SBS side, the whole sample was immersed into a water bath. Water immediately wet the sample through the micropores and dissolved the dextran layer (movie S1), and a free-standing Ag-coated SBS fiber mat was obtained in just a few minutes (Fig. 2A and movie S2). After drying, EGaIn was applied onto the SBS substrate. Because of the poor affinity to SBS and the high reactivity with Ag, EGaIn selectively dewets from the SBS surface and wets on the Ag-covered areas to form the μLMEs on the supersoft SBS fiber mat (Fig. 2B).

The success rate of pattern transfer is largely dependent on the penetration speed of water through the SBS fiber mat. We first characterized the intrinsic dissolving speed of the dextran (~1 nm/s) without the coverage of the stamp/receiver substrate (fig. S4). After covering an electrospun SBS fiber mat, the surface was initially hydrophobic with a large water contact angle of 130° (fig. S5). At this point, it took 2 min to wet the bottom substrate, and the dextran layer was difficult to be dissolved. After the plasma treatment (Fig. 2C), the SBS surface became superhydrophilic (movie S3). The penetration time decreased to 3 s when the plasma time was 20 min (fig. S6). Accordingly, the pattern transfer rate, which is defined by the area of transferred Ag features to the total patterned area, increased from almost zero (before plasma treatment) to above 95% (Fig. 2D and fig. S7). In contrast, samples covered with impermeable spin-coated SBS film did not show any trace of pattern transfer even after immersing in water for 1 week (fig. S8).

Note that the selectivity wetting of EGaIn lies in the reactive alloying between Ag and In to form AgIn alloys, which shows high affinity to additional EGaIn applied on top of the Ag area (fig. S9). Additional EGaIn applied on the surface will wet the as-formed AgIn alloy layer to form the trilayer of EGaIn/AgIn/Ag. The EGaIn contact angle reduced from 140° to 30° when the Ag layer increased from 0 to 300 nm (Fig. 2E). μLMEs with dimensions ranging from 2 to 1000 μm and a wide variety of shapes, including arbitrary patterns for various electrical components (lines, dots, source-drain electrode, interconnect, mesh electrode, antenna, generator, inductor, capacitor, and resistor), were obtained (figs. S10 and 11). We observed a slight widening of the EGaIn feature in comparison to the original Ag patterns. For instance, as shown in Fig. 2F, the linewidth of the Ag electrode on the SBS fiber mat was 3.2 μm. After wetting, the final linewidth of the EGaIn electrode was 3.3 μm. It should be noted that the pitch of the patterns remained unchanged. The linewidth of μLMEs showed a linear relationship with the linewidths of Ag with a slope of ~0.99 (Fig. 2G). Figure 2H shows a μLME-based electronic patch consisting of arbitrary polygons, and Fig. 2I shows high-density electronic components with a density of 75,500 electrodes/cm^2. When attaching the electronic patch to the skin, nearly no LM residues were observed with the loading pressure lower than 3.2 kPa, and a trace amount of LM residues was found until the loading pressure reached 12.8 kPa (fig. S12).

Permeability, biocompatibility, conductivity, and stretchability of μLMEs

Owing to the high porosity of the fiber mat, μLMEs have excellent permeability to air, moisture, and liquid (movie S4). Figure 3A showed the graduate penetration of a colored liquid from the upper side of the μLME to the bottom side, showing the outstanding liquid permeability. The air permeability and moisture permeability of μLMEs on a 330-μm-thick SBS fiber mat were 78 mm/s and 835 g/m^2 per day, respectively (Fig. 3, B and C). The values are similar to previous literature reports using similar thicknesses of testing materials and testing methods (18). In contrast, the air permeabilities of Ecoflex and PDMS thin films were almost zero. Their moisture permeabilities were below 50 g/m^2 per day. Moreover, the permeability of μLMEs could be further enhanced by decreasing the SBS thickness. At a thickness of 25 μm, the air permeability and the moisture permeability reached 235 mm/s and 990 g/m^2 per day, respectively. In addition, μLMEs had low cytotoxicity in the in vitro study by using L-929 cells as the model cell (fig. S13). Further, in vivo animal experiments on the rabbit skin denoted no obvious irritation (i.e., no erythema and oedema on the skin) during the observation period (24, 48, and 72 hours; fig. S14).

We characterized the conductivity of the μLMEs at different linewidths. When increasing the linewidth from 2 to 200 μm, the μLME pertained a high level of conductivity in the range of 1.3 to 3.9×10^5 S/cm (Fig. 3D and fig. S15). We noticed that the conductivity of μLMEs is higher than pristine EGaIn (lower than pristine Ag). We believe that this enhancement can be attributed to the contribution from the more conductive Ag layer underneath the LM (fig. S16). It should be also noted that, without LM, transferred Ag on the SBS fiber mat cannot sustain tensile strain over 50% with the presence of cracks ranging from several micrometers to several dozens of micrometers (fig. S17).

In contrast, μLMEs were highly stretchable and conductive. Because of the trilayer structure of LM/AgIn/Ag, the fluidic LM could well connect the broken solid metal on the fiber surface, forming a continuous conductive pathway. The resistance of the 5-μm μLME increased only by 0.6% at a tensile strain of 300% (Fig. 3E). When increasing the linewidth to 10 and 50 μm, μLMEs could show electrical stability at higher tensile strains, with resistance increasing by only 1.3 and 1.1 folds at 1000% strain, respectively. When increasing the linewidth to 200 μm, the
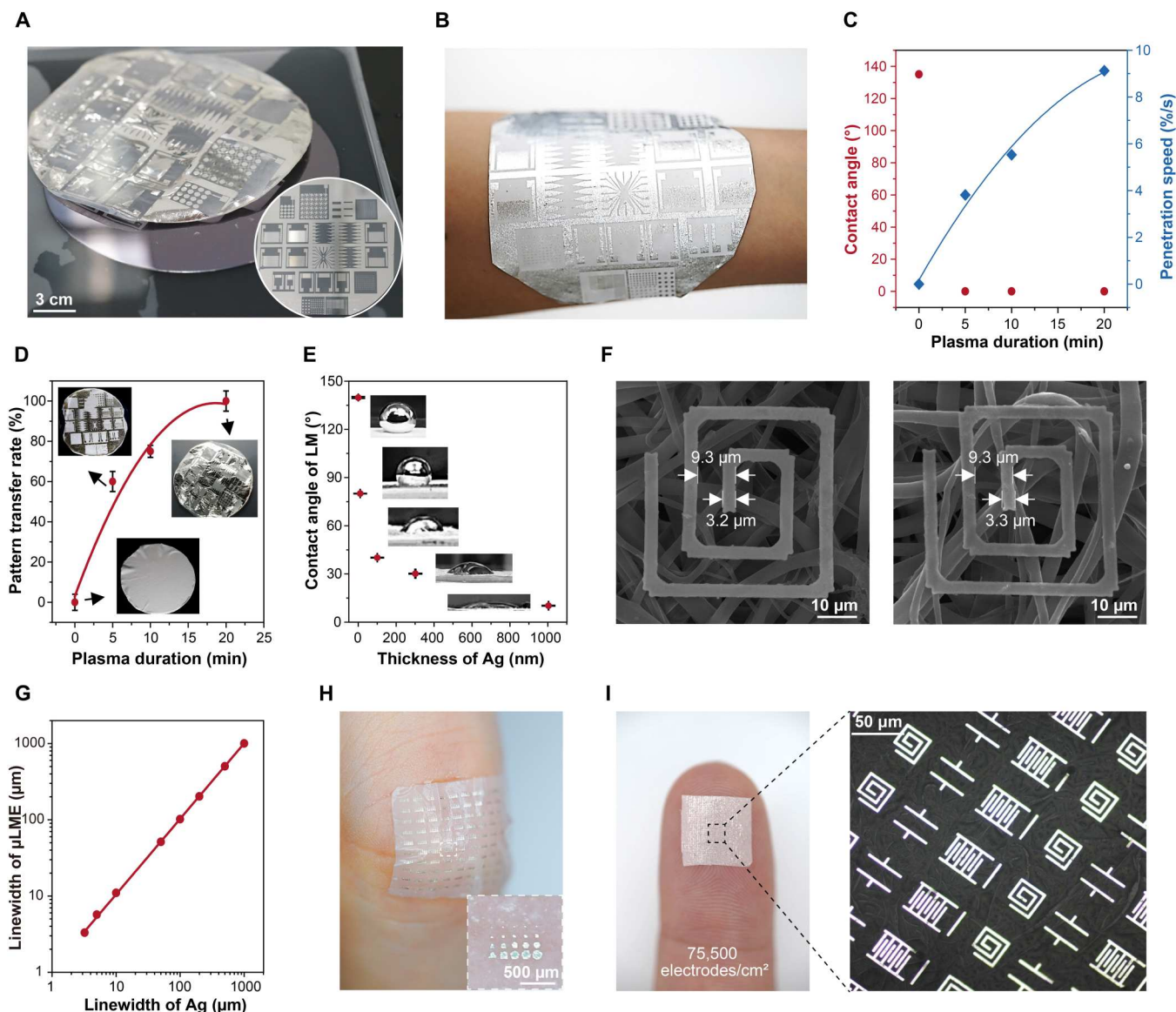
Fig. 2. Structures of μLMEs. (**A**) Digital images showing the transfer of Ag micropatterns from the wafer to the SBS fiber mat. The inset image shows the wafer-sized Ag micropatterns patterned on the wafer before transfer. The main image shows the transferred Ag onto the SBS fiber mat after dissolving the sacrificial layer. The supersoft and freestanding sample is floating on the water. (**B**) Digital image of μLMEs attached on a human arm (mass loading of LM, 10 mg/cm²). (**C**) Contact angle and penetration speed of the solvent to the sacrificial layer and (**D**) the pattern transfer success rate as a function of the plasma duration. (**E**) Contact angle of LM on the transferred Ag layer as a function of the Ag thicknesses. (**F**) Scanning electron microscopy images showing an electrode on the SBS fiber mat before and after the selective wetting with LM. (**G**) Summary of the linewidths of μLMEs in correspondence to the original linewidths of Ag electrodes. (**H** and **I**) Digital images of high-density μLMEs with a density as high as 75,500 electrodes/cm².

resistance only changed by 5.25 folds at a strain of 1500%. Moreover, μLMEs with various linewidths (10, 50, and 200 μm) showed electrical stability and robustness during stretch-release cyclic tests under large strains (>1000% strain) (Fig. 3F and fig. S18), resulting from the formation of the reversible buckling structure (fig. S19). These buckles are formed because of the formation of a thin solid layer of Ga_2O_3 on the LM surface. Since the oxide layer is much harder than the LM, buckles formed as a consequence of the mechanical competition between the harder upper oxide layer and the softer underlying substrate. Such a buckled structure benefits the outstanding stretchability and electrical stability of μLMEs.

The resistances of μLMEs changed only by 1.03 (linewidth, 10 μm) after 100 cycles and 0.393 folds (linewidth, 50 μm) after 500 cycles of stretch-release tests at a strain of 1000%.

μLME-based implantable bioelectronics for neural interface with chronic biocompatibility

Owing to the attributes of super-softness, biocompatibility, stretchability, and high spatiotemporal resolution, μLMEs are suitable for implantable bioelectronics where high device density and chronic comfortability are critically important (*16*, *61*). As a proof of concept, we fabricated an implantable μLME array for the recording
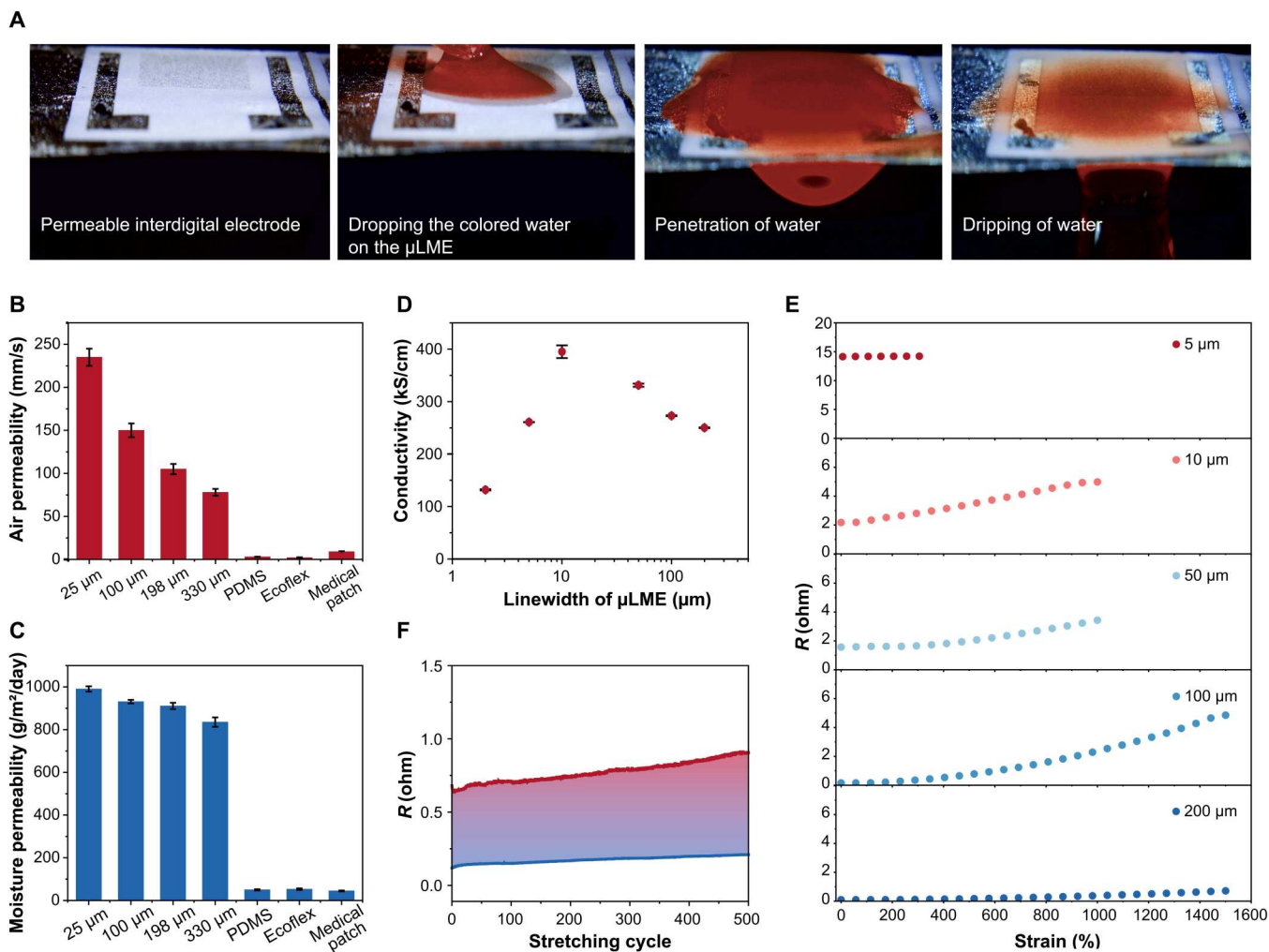
Fig. 3. Permeability, conductivity, and stretchability of µLMEs. (**A**) Digital images showing the penetration of one colored water droplet from one side of µLMEs to the other side. (**B** and **C**) Air and moisture permeability of µLMEs on SBS mats with various thicknesses, as well as other common substrates for bioelectronics including PDMS, Ecoflex, and medical patch. (**D**) Electrical conductivity of µLMEs of various linewidths. (**E**) Resistance (R) of µLMEs of various linewidths at different tensile strains. (**F**) Cyclic electrical stability of µLMEs (linewidth, 50 µm) under a large tensile strain of 1000%.

of ECoG signals from the soft, curved, and sophisticated neural interface. Major cortical subdomains of the rat consisting of motor, somatosensory, visual, and retrosplenial cortices were covered with the µLME array (Fig. 4A). The µLME array featured with a small diameter of the circular electrode unit (500 µm), fine interconnects (40 µm), and a high channel density of 100 electrodes/ cm^2 (fig. S20). Because of the similarity in mechanical compliance with the brain tissue (fig. S21), µLME (thickness, 25 µm) was conformally attached to the cortical surface (Fig. 4, B and C), which showed a much lower low Young's modulus (Fig. 4D) and superior conformability (fig. S22) compared with reported electrode materials for ECoG devices (e.g., Au/PI, Au/parylene, and silicon).

To verify the possibility of µLME array for neural electrophysiological recording and stimulation, in vitro electrochemical impedance characterization was first carried out. The electrochemical impedance of the µLME interface in phosphate-buffered saline (PBS) was similar to that of the commonly used Au/PI electrode with the same dimension in the frequency ranges from 1 to

10,000 Hz. The µLME array could be readily stretched up to 500% and maintained good stability of the impedance and phase signals, while the Au/PI electrode showed marked changes when stretched up to 30% (Fig. 4E and fig. S23). In addition, the 36-channel µLME array showed a low variation of the electrochemical impedance among individual electrodes (fig. S24).

For in vivo recording of the cortical activity, we recorded the neural signal of the rat during sleeping (fig. S25). From the power spectrum of the signal, the nonrapid eye movement sleep of the rat was observed, which is associated with the existence of low-frequency delta waves lower than 4 Hz and theta waves ranging from 4 to 8 Hz (Fig. 4F). To verify the capability of the µLME for recording region-specific cortical activity, we stimulated the forelimbs with short electric current pulses and examined the induced somatosensory evoked potentials (SEPs) in the cortex. The SEPs were recorded under electrical stimulations with frequencies ranging from 1 to 9 Hz (Fig. 4G) and pulse voltages ranging from 1 to 6 V (Fig. 4H), respectively. The amplitude of the neural signal displayed an
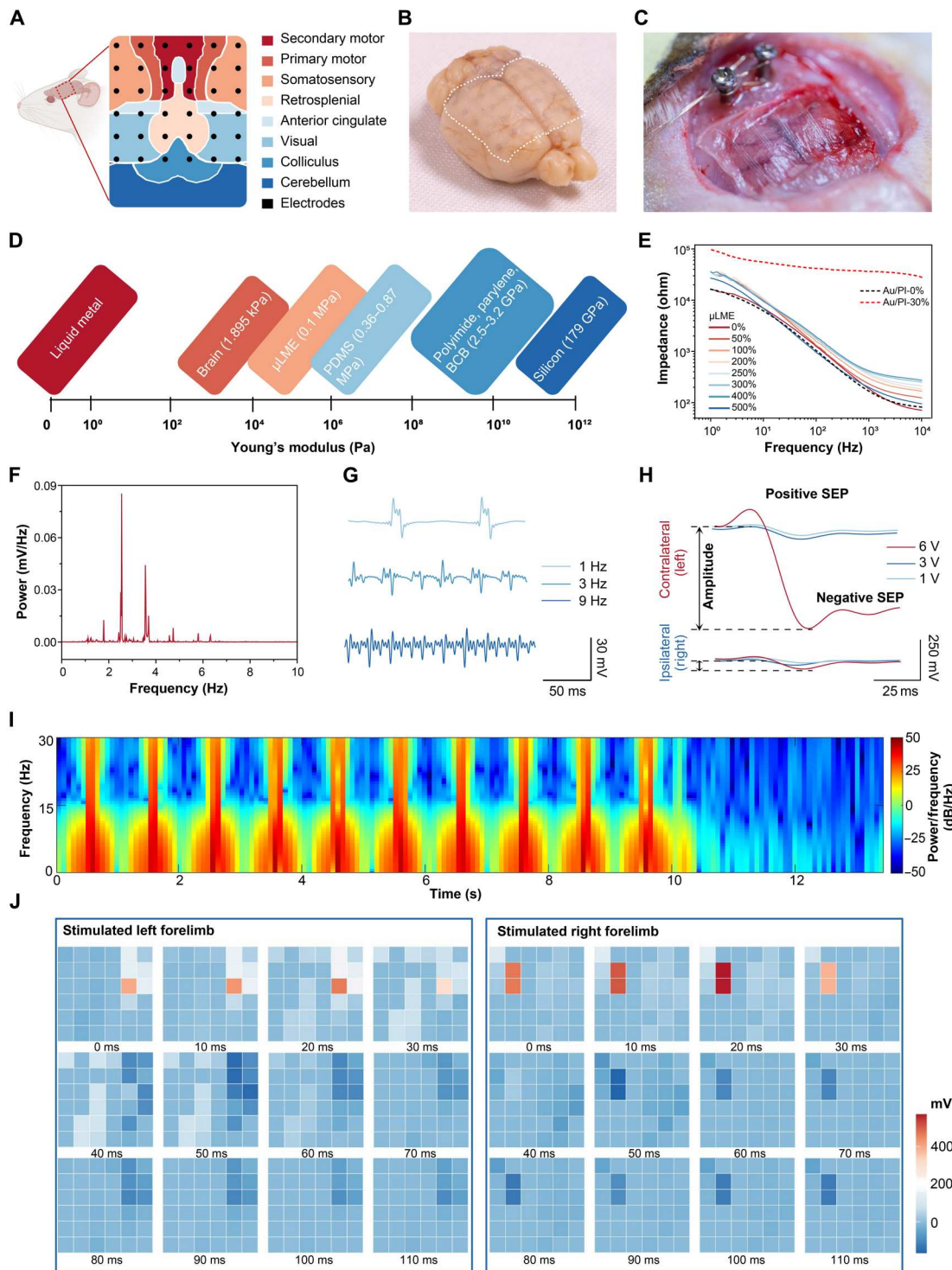
Fig. 4. High-density μLMEs-based bioelectronics for the neural electrophysiological interface. (**A**) Schematic illustration showing the application of μLMEs-based ECoG array and the recorded cortical subdomains. (**B** and **C**) Digital images of μLME ECoG electrode array (thickness, 25 μm) with conformal attachment onto the soft, curved, and sophisticated cerebral cortex. The dashed line showed the boundary of the μLME array. (**D**) Comparison of Young's modulus of μLMEs with reported materials for ECoG bioelectrodes. (**E**) In vitro electrochemical impedance spectroscopy (EIS) characterizations of μLMEs and Au/PI electrodes under different strains. (**F**) Power spectrum analysis of in vivo neural signals at the sleep state of a living rat. (**G**) Somatosensory evoked potentials (SEPs) recorded with μLMEs under electrical stimulations with pulse voltage of various frequencies. (**H**) Comparison of SEPs in the contralateral and ipsilateral somatosensory cortices under electrical stimulations with pulse voltage of various intensities. (**I**) Spectrogram of the signals of the contralateral somatosensory cortex under 10 continuous electrical stimulations with the intensity of 6 V and the frequency of 1 Hz. (**J**) Spatiotemporal properties for the μLME array in response to the electrical stimulations of left and right forelimbs.

intensity-dependent manner, from 15 to 107 mV in the positive SEPs and 44 to 630 mV in the negative SEPs with increasing pulse voltage. Notably, the neural signals in the contralateral (left) hemispheres were much stronger than those in the ipsilateral (right) hemisphere since these electrical stimulations were applied on the right forelimb (Fig. 4H). Moreover, rhythms (7 to 14 Hz) of the ECoG signals were observed reproducibly throughout 10 continuous electrical stimulations (Fig. 4I).

Figure 4J shows the analysis of the spatiotemporal properties for the μLME array. In response to forelimb stimulations, peak values of positive SEPs (colored red regions) were detected at ~20 ms on the stimulated hemispheres after stimulation onsets of both forelimbs, whereas the counterpart hemispheres lacked these responses. In contrast, negative SEP (colored dark-blue regions) peaks emerged in both hemispheres, representing a cognitive response to the stimulus. Other cortical areas such as motor (primary and secondary) cortexes and visual cortex also showed weaker SEP signals compared with the somatosensory cortex.

The μLME array showed outstanding chronic biocompatibility that is important for chronic implantation. Right after the implantation, no damage or inflammatory responses were found in the tissues and cells from the immunohistological analysis of the brain slice (Fig. 5A). After implantation for 2 and 32 weeks, the microglial activation level in the μLME groups still showed no significant difference from the control group in both soma size and Ionized calcium binding adaptor molecule 1 (Iba1) number (Fig. 5B). In contrast, implantation using Au/PI and Au/PDMS for 2 weeks showed a significantly increased soma size of the microglia and the amount of the Iba1 in comparison to the control ($P <$ 0.001, t test), indicating a significant microglial activation and inflammation response (Fig. 5, C and D). Last but not least, the implanted μLMEs have chronic biocompatibility in living rats over a period of 8 months compared with current ECoG devices (table S1). μLME also showed superior biocompatibility to Au/PI and Au/PDMS when these samples were implanted in the skeletal muscle of rats for 1 week (fig. S26). The superiority is most likely resulted from the improved softness, stretchability, and permeability of the μLMEs. We also explored long-term electrical stability of μLMEs in the air and in PBS solutions (fig. S27). We fabricated two types of μLME electrodes as shown in fig. S27A, including (i) μLMEs without encapsulation and (ii) partially encapsulated μLMEs in which the leads and contact pads are encapsulated with another layer of SBS fiber mat. The μLMEs showed outstanding electrical stability in the air even without encapsulation, and the electrical resistance only changed by 0.45% after 100 hours (fig. S27B). When tested in PBS solutions, μLMEs without encapsulation showed good stability for up to 7.5 hours, but then the electrical resistance went up suddenly, indicating a disconnection between the measuring wire and the μLMEs due to corrosion of the LM (fig. S27C). In contrast, the electrical resistance of the partially encapsulated sample remained stable in the 100-hour test (fig. S27D). For the impedance test in PBS solutions, the μLMEs without encapsulation also showed poor stability (fig. S27E), and the impedance went up by one order of magnitude after testing for 8 hours. The impedance of the partially encapsulated μLMEs remained good stability (fig. S27F). The results show that there is indeed a slow corrosion of the impedance without encapsulation.

DISCUSSION

Porous and stretchable substrates such as electrospun fiber mats have outstanding permeability, softness, and biocompatibility, which are critical attributes for bioelectronic applications. However, different from planar substrates such as thin-film plastics or elastomers that are the main choices nowadays (table S2) (32–41), patterning high-resolution electrodes on rough, porous substrates has been a challenging task. The patterning process is majorly carried out by printing methods such as screen printing and inkjet printing or shadow mask methods. Hence, the patterning resolution has been limited to 50 to 10,000 μm (18, 26, 27, 62), so the device density was very low (table S3).

The successful preparation of μLMEs over a large-size, permeable, and stretchable fiber mat paves the way toward high-density, integrated, implantable, and chronically biocompatible LM electronics. At this moment, μLMEs display a typical patterning resolution of 2 μm by laboratory-equipped photolithography, moisture permeability of 990 g/m^2 per day, device density over 75,000 electrodes/cm^2, electrical conductivity in the order of 10^5 S/cm, and stretchability up to 1500% strain. In principle, the patterning resolution of μLMEs can be further enhanced to submicrometer (0.25 to 1 μm) regions, e.g., by using a high-resolution lithographic tool and fiber mat of smaller fiber diameters (fig. S28).

MATERIALS AND METHODS
Materials
Solvents including acetone, tetrahydrofuran, dimethylformamide, ethanol, and 2-propanol were purchased from Anaqua Global International Inc. Limited. The negative photoresist (NR9-1500P) and the developer for NR9-1500P (DR6) were obtained from Futurrex Inc., USA. LM and dextran were purchased from Sigma-Aldrich and used as received. All materials were used as received.

Fabrication of the permeable and μLMEs
A Si or SiO$_2$ wafer was first sonicated in acetone, 2-propanol, and deionized (DI) water, respectively, and then was blown dried with nitrogen gas. After that, a dextran solution (10 wt % in water) was spin-coated on the wafer at 4000 rpm for 40 s to form a sacrificial layer, followed by a baking treatment on a hotplate at 80°C for 1 min and 180°C for 30 min. The baked dextran-coated wafer was subsequently spin-coated with a layer of negative photoresist NR9-1500P at 4000 rpm for 40 s, followed by a prebaking treatment on a hotplate at 155°C for 1 min. The photoresist was then exposed to ultraviolet (UV) light with a dose of 170 mJ/cm^2 with the assistance of a mask aligner (Suss MA6). After the UV exposure, the photoresist was postbaked at 105°C for 3 min and then developed in DR6 developer for 10 to 15 s. After rinsing the sample in DI water and drying with compressed nitrogen gas, a 300-nm-thick Ag layer was deposited onto the wafer by the thermal evaporation method. Subsequently, the lift-off process was carried out in the acetone solvent to form the Ag micropatterns on the wafer. To transfer the Ag micropatterns to the stretchable and permeable fibrous substrates, SBS fiber mat with a thickness ranging from 25 to 330 μm was directly electrospun on the surface of the wafer deposited with Ag micropatterns, followed by plasma treatment for 20 min. The plasma treatment (Harrick, radio frequency power 18W) involved the use of air with a flow rate of around 0.5 standard cubic feet
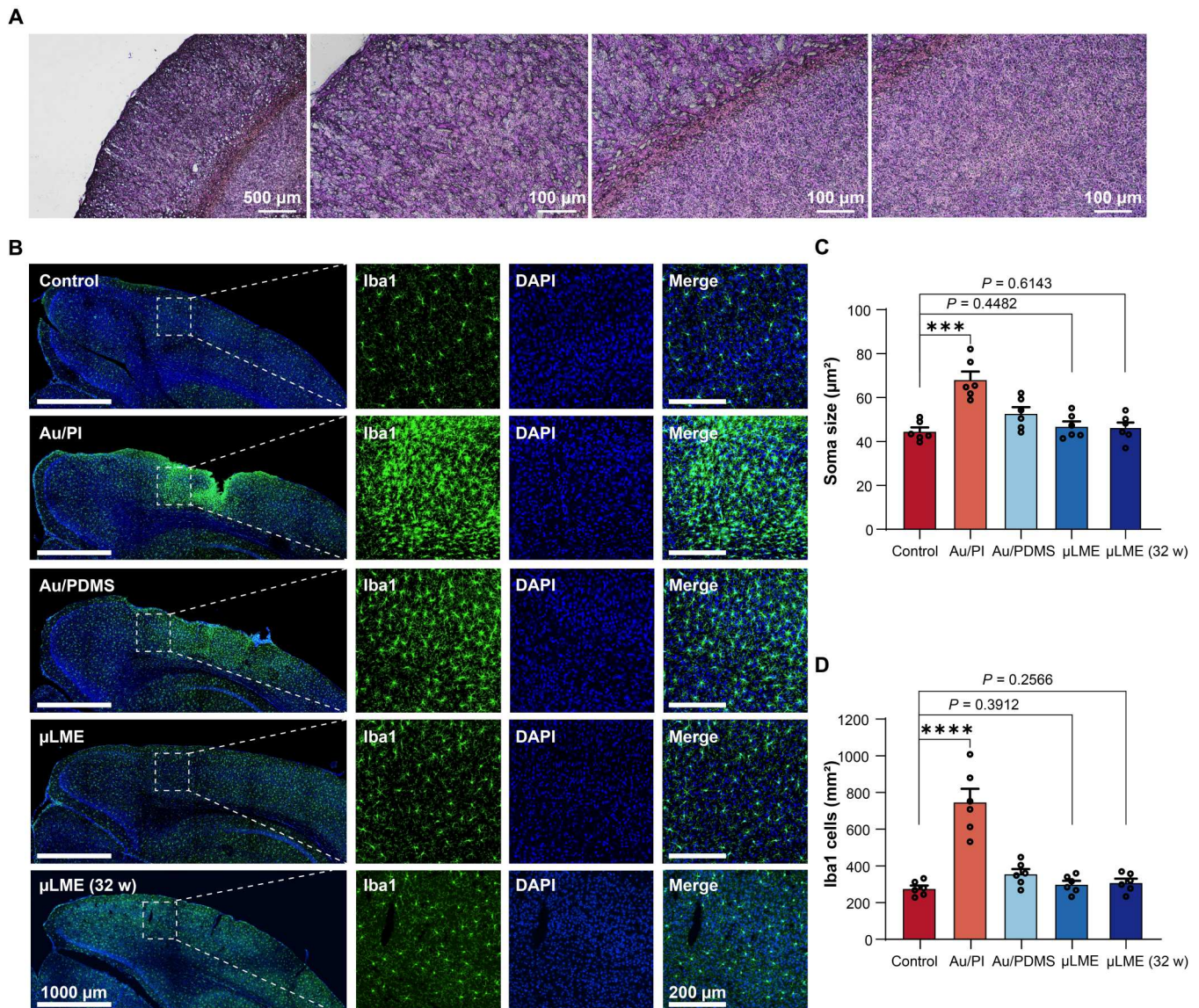
Fig. 5. Chronic (long-term) biocompatibility of μLMEs for chronic neural implants. (**A**) Immunohistological analysis of a stained brain slice after implantation of the electrode array for 2 hours. (**B**) Immunohistochemistry staining of the microglia (Iba1, green) and nuclei [4′,6-diamidino-2-phenylindole (DAPI), blue] at 2 weeks post-implantation of the control, Au/PI electrodes, Au/PDMS electrodes, μLME electrodes, and μLME electrodes with the implantation duration of 32 weeks (32 w). The left shows the low-magnification pictures (scale bars = 1000 μm), and the right shows the high-magnification ones (scale bars = 200 μm). (**C**) Statistical analysis of the microglia soma size ($n = 6$). A significant increase in soma size was found in the Au/PI group ($P = 0.0002$) and Au/PDMS group ($P = 0.0375$) compared to the control (two-way, unpaired Student's t test). No significant difference was found between the μLME groups and the control group ($P = 0.4482$ at 2 weeks postimplantation, $P = 0.6143$ at 32 weeks postimplantation). (**D**) Statistical analysis of the total microglia cells intensity ($n = 6$). A significant increase in iba1 cells was found in the Au/PI group ($P < 0.0001$) and Au/PDMS group ($P = 0.0274$) compared to the control (two-way, unpaired Student's t test). No significant difference was found between the μLME groups and the control group ($P = 0.3912$ at 2 weeks postimplantation, $P = 0.2566$ at 32 weeks postimplantation).

per hour and a pressure of 200 mTorr. Then, the sacrificial layer between the wafer and the Ag micropatterns was dissolved by immersing the sample in the DI water within minutes at room temperature. The SBS fiber mat was peeled off from the wafer, and the Ag micropatterns were transferred to the fiber mat. To obtain μLMEs, LM was applied to the Ag micropatterns by selective wetting in a glovebox filled with Ar gas.

Measurement of the water penetration speed through the SBS fiber mats

The penetration speed of the water through the SBS fiber mat was reflected by the water contact angle, wetting time, wetting radius, and absorption speed. The contact water angle on the SBS fiber mat plasma treated with different durations was measured by a contact angle measurement instrument (SDC-350). The drop amount of the water was fixed as 5 μl. The wetting time, wetting radius, and absorption rate of water were measured by the Moisture

Management System (SDL Atlas) according to the standard of the American Association of Textile Chemists and Colorists 79.

Characterizations of the morphology and permeability of μLMEs

The morphology and surface roughness of the sacrificial layer were characterized by the atomic force microscope (XE 70). The line-widths and thicknesses of μLMEs were determined by the three-dimensional optical surface profiler (New Zygo NexView). The surface morphology and elemental mapping of the samples were collected by scanning electron microscopy (TESCAN VEGA3). The air permeability tests were conducted according to ASTM D737-08 standard using a MO21S air permeability tester (SDL Americ Inc.). The pressure of the airflow was set at 100 kPa. Moisture permeability tests were performed according to the standard E96/E96M-13 by the cup method. The testing duration was 72 hours. Both air permeability and moisture permeability tests were performed at constant temperature (22°C) and humidity (63%).

Electrical and mechanical characterizations of μLMEs

The electrical conductivity (σ) of μLMEs was calculated according to the formula $\sigma = L/(A \times R)$, where L, A, and R are the length, cross-sectional area, and electrical resistance of the μLME, respectively. A of μLMEs was determined by the surface profiler (New Zygo NexView) (fig. S9), and the integrated polygon area was calculated using the software OriginPro 8.5. R values of the μLMEs with different linewidths ($L = 10$ mm) were measured via DC I-V characteristics with a parameter analyzer (Keithley 4200A-SCS Parameter Analyzer) connected with a probe station (Micromanipulator) (fig. S13). The electrical resistance of μLMEs under different strains was measured by a four-terminal method with a source meter (Keithley 2400) coupled with a customized stretching machine (Precise). The loading pressure for observing the LM residues on the skin was applied using a compression dynamometer (Handpi instruments).

Electrochemical characterizations

Electrochemical impedance spectroscopy (EIS) was conducted using an electrochemical workstation (CHI 660E) with a three-electrode testing system. Ag/AgCl (2 M KCl), platinum foil, and the μLME were performed as the reference electrode, counter electrode, and working electrode, respectively. PBS solution (1×; Gibco) was used as the electrolyte. Impedance and phase angle as a function of frequency ranging from 1 to 10,000 Hz were recorded by an AC sinusoid signal amplitude of 10 mV. The EIS spectra of μLMEs stretched with various strains were acquired with the same electrochemical workstation coupled with a homemade stretching setup.

Rat surgery

All procedures following the animal studies and the experimental protocols were reviewed and approved by the Animal Research Ethics Sub-Committee, Research Committee at the City University of Hong Kong (approval number A-0664). Male Sprague Dawley rats were ordered from the Laboratory Animal Services Centre, Chinese University of Hong Kong (aged 7 to 8 weeks, 200 to 300 g). All rats were housed in the Laboratory Animal Research Unit, City University of Hong Kong, under 12-hour/12-hour light/dark cycles until experiments. Before the surgery, the rats were first anesthetized with gaseous isoflurane (2 liters/min air mixed with 3% isoflurane) and then deeply anesthetized with pentobarbital sodium

(30 mg/kg). After anesthesia, the rat head was shaved under 37°C. The midline skin incision was first made over the craniovertebral junction. The overlying muscles were then cut and retracted to expose the skull. A craniotomy was performed using a dental drill, and then the dura was peeled off using a fine tweezer to ensure full exposure of the cerebral cortex.

ECoG neural signal recording and electrical stimulations

The μLME array bonded on a flexible printed circuit (FPC) connector was connected to a printed circuit board with a customized FPC adaptor, and then ECoG neural signals were recorded with a multichannel high-precision data acquisition system (PowerLab 16-35, AD Instruments). Signals were acquired and digitally band-pass filtered (1 to 30 Hz) by matched software LabChart. Sequential electrical stimulations were performed on both the left and right forelimbs of the rat using square wave voltage pulses with various applying frequencies (1, 3, and 9 Hz) and intensities (1, 3, and 6 V) generated by the stimulation output port of the PowerLab through a Bayonet Neill–Concelman cable. A total of 50 pulses were delivered at a frequency of 1 Hz for each stimulus condition, and 50 responses per stimulus condition were averaged. A custom MATLAB code was adopted for analyzing the spectrogram of the ECoG neural signals.

Cryosection, histological staining, and observations of the brain slice

After the implantation of the μLME array, the histological status of the brain slice was first studied. To protect the tissular structure, the specimen was fixed in a PBS solution with 4 wt % formaldehyde for 24 hours and transferred into 30% sucrose solution overnight, after which it was transferred to sucrose-cryo–optimal cutting temperature media compound before frozen sectioning. Then, the brain specimen was frozen at −80°C and sliced with the freezing microtome (CryoStar NX70) with a block thickness of 15 μm. The hematoxylin and eosin (H&E) staining method was adopted by using the basic dye hematoxylin (BL 735A-1) for the staining of acidic cell components (i.e., nucleic acids, glycosaminoglycans, and acid glycoproteins) and the acidic dye eosin (BL 735B) for the staining of the cell cytoplasm. Specifically, the slices were first stained with hematoxylin solution for 5 min after cleaning with DI water. Then, the slices were thoroughly rinsed in DI water, followed by differentiation in the 0.1% acetic acid and 85% ethanol in water for 10 s and rinsed again with DI water for 1 min. Next, the slices were blued in the PBS/PBS with 0.05% Tween solution for 30 s and then rinsed with DI water. After washing the blued slice in ethanol for 10 s, eosin was also applied to stain the tissue for 30 s. Last, the slices were dehydrated in ethanol (95%) and permeabilized in xylene two times (5 min each), respectively. For immunohistochemical analysis, slices were observed with the invert microscope (Nikon Eclipse Ti).

Cell cytotoxicity test of μLMEs

Specimens for the cell cytotoxicity tests included the control sample (fresh full medium), absorbent gauze, SBS mat, μLME, and 20% dimethylsulfoxide (DMSO). L-929 cells (American Type Culture Collection, USA) were used to investigate the in vitro cytotoxicity of all the specimens following the ISO 10993-5:2009(E) standard. All the L-929 cells were seeded in the full Dulbecco's modified Eagle's medium (Hyclone, Hong Kong) supplemented with 10% fetal

bovine serum (Hyclone, Hong Kong) and 1% penicillin/streptomy-cin (Hyclone, Hong Kong) in a 24-well plate with the seeding density of cells 6×10^4/ml. After incubation for 24 hours and the verification of the cell confluency and morphology, the medium was discarded, and 1 ml of the fresh full medium was added to the culture plate. Next, 0.2-cm^2 sterile specimens were added to the 24-well plate to evaluate the cytotoxicity of the materials. All specimens were cultured at 37°C in an incubator with 5% CO_2. After discarding the culture medium, the staining solution containing 200 μl of PBS, 2 μM calcein AM, and 8 μM propidium iodide was added, followed by incubation for 45 min. Then, a fluorescent microscope (Zeiss, Germany) was used to observe the cells after rinsing them with PBS. To investigate the cell proliferation, 500 μl of 3-(4,5-Dimethylthiazol-2-yl)-2,5-Diphenyltetrazolium Bromide solution was added to each well followed by incubation for 2 hours. Next, 500 μl of DMSO was added to dissolve the formazan. The absorption at 450 nm denoting the cell metabolic activity was measured with a plate reader (BioTek, USA). The cell viability was calculated using the absorbance ratio between the tested well and the blank control well.

In vivo evaluation of irritation and skin sensitization of μLMEs

Animal experiments of the specimens were performed following the ISO 10993-10:2010(E) standard. All procedures followed the ethical guidelines for experimental animals, which were approved by The Hong Kong Polytechnic University. Four groups of samples were evaluated including negative control (thin cotton cloth) as group 1, positive control (thin cotton cloth rinsed with saturated sodium dodecyl sulfonate) as group 2, SBS mat as group 3, μLME with the serpentine structure as group 4. All samples were cut into 2.5 cm by 2.5 cm and then were attached to the New Zealand White Rabbits (weighing 2.0 to 3.0 kg). The backs of the rabbits were shaved in advance 24 hours before the attachment of the specimens. Each group had three sample patches, which were applied onto the skin underneath the gauze pads (2.5 cm by 2.5 cm) secured with the semi-occlusive medical sterile wound dressings (Hynaut, Tsing-tao, China). The patches were removed after exposure to the shaved skin for 24 hours. Then, the test sites were observed at 0 (initial), 24, 48, and 72 hours after sample attachment for visible changes like erythema. The mean erythema scores were measured on a scale from 0 to 4, in which grade 0 indicated no erythema, grade 1 indicated slight erythema, grade 2 indicated moderate erythema, grade 3 indicated moderate to severe erythema, and grade 4 indicated severe erythema.

Chronic (long-term) biocompatibility test of implanted μLMEs

For the biocompatibility test on the brain, we implanted the electrodes (μLME, Au/PI, and Au/PDMS with the same electrode design) into the cerebral cortex to evaluate their chronic biocompatibility. In this study, male Institute of Cancer Research mice (6 to 8 weeks, $n = 2$) were anesthetized with intraperitoneal injected ketamine (100 mg/kg) and xylazine (10 mg/kg) and fixed on a stereotaxic frame. As shown in fig. S29, the craniotomy was performed between the bregma and lambda of the skull anterior−posterior, −1.5 to −4.5; medial−lateral, 0.5 to 3.5. Three stainless bone screws were placed into the skull surrounding the surgical openings, and the dura mater was subsequently removed. Electrodes were put

over the left and right cortical surfaces, respectively. The craniotomy was filled with Kwik-Sil silicone elastomer (World Precision Instruments Inc.) and then coated with dental cement (Megadental, Germany) after the Kwik-Sil was cured. The mice were euthanized at 2 weeks and taken for immunohistological analysis to evaluate their biocompatibility. For mice with the implantation of μLMEs, the maximum implantation duration in this biocompatibility study is 32 weeks. We anesthetized the mice by intraperitoneal injection of ketamine (100 mg/kg) and xylazine (10 mg/kg) and then perfused the mice transcardially with PBS followed by 4% paraformadehyde (PFA). The brain samples were incubated in PFA overnight and then with 30% sucrose solution for 3 days. Brains were cryosectioned at a thickness of 30 μm. The slices were stained with Iba1 antibody (Abcam, ab178846) and 4′,6-diamidino-2-phenylindole (nuclei marker) and observed with laser confocal microscopy (Nikon A1HD25, Japan). The regions of interest for the assessment of intensity and soma size of Iba1-positive cells were chosen from the electrode-brain interface to the tissues 600 μm beneath the interface (three slices for each mouse). We analyzed the intensity and soma size of Iba1-positive cells using ImageJ software. For investigating the chronic biocompatibility of various electrodes in the biceps femoris muscle, healthy male Sprague Dawley rats (aged 4 to 5 weeks, 200 g) were used for biceps femoris muscle implantation. The Dawley rats were first treated with gaseous light anesthesia (isoflurane), followed by the injection of ketamine (1 wt %) for deep anesthesia. Then, a required wound (6 mm in width and 2 mm in depth) was created, with the attachment of the electrode array (μLME, Au/PI, and Au/PDMS) on the surface of the biceps femoris muscle. After suturing and implanting for 1 week, the samples were collected and frozen sectioned (25 μm thick) using CryoStar NX70 Cryostat (Thermo Fisher Scientific). Stained by the H&E (Abcam) method, the slices were later observed with an inverted microscope (NikonTi2-A).

Supplementary Materials

This PDF file includes:
Supplementary Text
Figs. S1 to S29
Tables S1 to S3
Legends for movies S1 to S4
References

Other Supplementary Material for this manuscript includes the following:
Movies S1 to S4

REFERENCES AND NOTES

1. Y. Wang, H. Haick, S. Guo, C. Wang, S. Lee, T. Yokota, T. Someya, Skin bioelectronics towards long-term, continuous health monitoring. *Chem. Soc. Rev.* **51**, 3759–3793 (2022).
2. C. Wang, X. Chen, L. Wang, M. Makihata, H.-C. Liu, T. Zhou, X. Zhao, Bioadhesive ultrasound for long-term continuous imaging of diverse organs. *Science* **377**, 517–523 (2022).
3. H. Yuk, B. Lu, X. Zhao, Hydrogel bioelectronics. *Chem. Soc. Rev.* **48**, 1642–1667 (2019).
4. Y. Yang, W. Gao, Wearable and flexible electronics for continuous molecular monitoring. *Chem. Soc. Rev.* **48**, 1465–1491 (2019).
5. Y. S. Choi, H. Jeong, R. T. Yin, R. Avila, A. Pfenniger, J. Yoo, J. Y. Lee, A. Tzavelis, Y. J. Lee, S. W. Chen, H. S. Knight, S. Kim, H. Y. Ahn, G. Wickerson, A. Vázquez-Guardado, E. Higbee-Dempsey, B. A. Russo, M. A. Napolitano, T. J. Holleran, L. A. Razzak, A. N. Miniovich, G. Lee, B. Geist, B. Kim, S. Han, J. A. Brennan, K. Aras, S. S. Kwak, J. Kim, E. A. Waters, X. Yang, A. Burrell, K. S. Chun, C. Liu, C. Wu, A. Y. Rwei, A. N. Spann, A. Banks, D. Johnson, Z. J. Zhang, C. R. Haney, S. H. Jin, A. V. Sahakian, Y. Huang, G. D. Trachiotis, B. P. Knight, R. K. Arora,

I. R. Efimov, J. A. Rogers, A transient, closed-loop network of wireless, body-integrated devices for autonomous electrotherapy. *Science* **376**, 1006–1012 (2022).

6. H. Lee, T. K. Choi, Y. B. Lee, H. R. Cho, R. Ghaffari, L. Wang, H. J. Choi, T. D. Chung, N. Lu, T. Hyeon, S. H. Choi, D. H. Kim, A graphene-based electrochemical device with thermoresponsive microneedles for diabetes monitoring and therapy. *Nat. Nanotechnol.* **11**, 566–572 (2016).

7. K. W. Cho, S. H. Sunwoo, Y. J. Hong, J. H. Koo, J. H. Kim, S. Baik, T. Hyeon, D. H. Kim, Soft bioelectronics based on nanomaterials. *Chem. Rev.* **122**, 5068–5143 (2022).

8. X. Yu, X. Xie, Y. Yu, J. Lee, A. Vazquez-Guardado, H. Luan, J. Ruban, X. Ning, A. Akhtar, D. Li, B. Ji, Y. Liu, R. Sun, J. Cao, Q. Huo, Y. Zhong, C. M. Lee, S. Y. Kim, P. Gutruf, C. Zhang, Y. Xue, Q. Guo, A. Chempakasseril, P. Tian, W. Lu, J. Y. Jeong, Y. J. Yu, J. Cornman, C. S. Tan, B. H. Kim, K. H. Lee, X. Feng, Y. Huang, J. A. Rogers, Skin-integrated wireless haptic interfaces for virtual and augmented reality. *Nature* **575**, 473–479 (2019).

9. J. A. Rogers, T. Someya, Y. Huang, Materials and mechanics for stretchable electronics. *Science* **327**, 1603–1607 (2010).

10. T. Someya, Z. Bao, G. G. Malliaras, The rise of plastic bioelectronics. *Nature* **540**, 379–385 (2016).

11. N. Matsuhisa, X. Chen, Z. Bao, T. Someya, Materials and structural designs of stretchable conductors. *Chem. Soc. Rev.* **48**, 2946–2966 (2019).

12. K. Sim, Z. Rao, F. Ershad, C. Yu, Rubbery electronics fully made of stretchable elastomeric electronic materials. *Adv. Mater.* **32**, 1902417 (2020).

13. Y. Jiang, Z. Zhang, Y. X. Wang, D. Li, C. T. Coen, E. Hwaun, G. Chen, H. C. Wu, D. Zhong, S. Niu, W. Wang, A. Saberi, J. C. Lai, Y. Wu, Y. Wang, A. A. Trotsyuk, K. Y. Loh, C. C. Shih, W. Xu, K. Liang, K. Zhang, Y. Bai, G. Gurusankar, W. Hu, W. Jia, Z. Cheng, R. H. Dauskardt, G. C. Gurtner, J. B. H. Tok, K. Deisseroth, I. Soltesz, Z. Bao, Topological supramolecular network enabled high-conductivity, stretchable organic bioelectronics. *Science* **375**, 1411–1417 (2022).

14. M. Lin, H. Hu, S. Zhou, S. Xu, Soft wearable devices for deep-tissue sensing. *Nat. Rev. Mater.* **7**, 850–869 (2022).

15. S. Liu, Y. Rao, H. Jang, P. Tan, N. Lu, Strategies for body-conformable electronics. *Matter.* **5**, 1104–1136 (2022).

16. E. Song, J. Li, S. M. Won, W. Bai, J. A. Rogers, Materials for flexible bioelectronic systems as chronic neural interfaces. *Nat. Mater.* **19**, 590–603 (2020).

17. A. Miyamoto, S. Lee, N. F. Cooray, S. Lee, M. Mori, N. Matsuhisa, H. Jin, L. Yoda, T. Yokota, A. Itoh, M. Sekino, H. Kawasaki, T. Ebihara, M. Amagai, T. Someya, Inflammation-free, gas-permeable, lightweight, stretchable on-skin electronics with nanomeshes. *Nat. Nanotechnol.* **12**, 907–913 (2017).

18. Z. Ma, Q. Huang, Q. Xu, Q. Zhuang, X. Zhao, Y. Yang, H. Qiu, Z. Yang, C. Wang, Y. Chai, Z. Zheng, Permeable superelastic liquid-metal fibre mat enables biocompatible and monolithic stretchable electronics. *Nat. Mater.* **20**, 859–868 (2021).

19. J. C. Doloff, O. Veiseh, R. de Mezerville, M. Sforza, T. A. Perry, J. Haupt, M. Jamiel, C. Chambers, A. Nash, S. Aghlara-Fotovat, J. L. Stelzel, S. J. Bauer, S. Y. Neshat, J. Hancock, N. A. Romero, Y. E. Hidalgo, I. M. Leiva, A. M. Munhoz, A. Bayat, B. M. Kinney, H. C. Hodges, R. N. Miranda, M. W. Clemens, R. Langer, The surface topography of silicone breast implants mediates the foreign body response in mice, rabbits and humans. *Nat. Biomed. Eng.* **5**, 1115–1130 (2021).

20. J. W. Salatino, K. A. Ludwig, T. D. Y. Kozai, E. K. Purcell, Glial responses to implanted electrodes in the brain. *Nat. Biomed. Eng.* **1**, 862–877 (2017).

21. Q. Huang, Z. Zheng, Pathway to developing permeable electronics. *ACS Nano* **16**, 15537–15544 (2022).

22. F. Chen, Q. Huang, Z. Zheng, Permeable conductors for wearable and on-skin electronics. *Small Struct.* **3**, 2100135 (2022).

23. L. Tian, B. Zimmerman, A. Akhtar, K. J. Yu, M. Moore, J. Wu, R. J. Larsen, J. W. Lee, J. Li, Y. Liu, B. Metzger, S. Qu, X. Guo, K. E. Mathewson, J. A. Fan, J. Cornman, M. Fatina, Z. Xie, Y. Ma, J. Zhang, Y. Zhang, F. Dolcos, M. Fabiani, G. Gratton, T. Bretl, L. J. Hargrove, P. V. Braun, Y. Huang, J. A. Rogers, Large-area MRI-compatible epidermal electronic interfaces for prosthetic control and cognitive monitoring. *Nat. Biomed. Eng.* **3**, 194–205 (2019).

24. B. Sun, R. N. McCay, S. Goswami, Y. Xu, C. Zhang, Y. Ling, J. Lin, Z. Yan, Gas-permeable, multifunctional on-skin electronics based on laser-induced porous graphene and sugar-templated elastomer sponges. *Adv. Mater.* **30**, 1804327 (2018).

25. W. Zhou, S. Yao, H. Wang, Q. Du, Y. Ma, Y. Zhu, Gas-permeable, ultrathin, stretchable epidermal electronics with porous electrodes. *ACS Nano* **14**, 5798–5805 (2020).

26. S. Lee, S. Franklin, F. A. Hassani, T. Yokota, M. O. G. Nayeem, Y. Wang, R. Leib, G. Cheng, D. W. Franklin, T. Someya, Nanomesh pressure sensor for monitoring finger manipulation without sensory interference. *Science* **370**, 966–970 (2020).

27. Q. Zhuang, Z. Ma, Y. Gao, Y. Zhang, S. Wang, X. Lu, H. Hu, C. Cheung, Q. Huang, Z. Zheng, Liquid–metal-superlyophilic and conductivity–strain-enhancing scaffold for permeable superelastic conductors. *Adv. Funct. Mater.* **31**, 2105587 (2021).

28. Q. Li, G. Chen, Y. Cui, S. Ji, Z. Liu, C. Wan, Y. Liu, Y. Lu, C. Wang, N. Zhang, Y. Cheng, K. Q. Zhang, X. Chen, Highly thermal-wet comfortable and conformal silk-based electrodes for on-skin sensors with sweat tolerance. *ACS Nano* **15**, 9955–9966 (2021).

29. X. Ma, M. Zhang, J. Zhang, S. Wang, S. Cao, Y. Li, G. Hu, D. Kong, Highly permeable and ultrastretchable liquid metal micromesh for skin-attachable electronics. *ACS Mater. Lett.* **4**, 634–641 (2022).

30. J. Xue, T. Wu, Y. Dai, Y. Xia, Electrospinning and electrospun nanofibers: Methods, materials, and applications. *Chem. Rev.* **119**, 5298–5415 (2019).

31. Y. Wang, T. Yokota, T. Someya, Electrospun nanofiber-based soft electronics. *NPG Asia Mater.* **13**, 22 (2021).

32. T. Lu, E. J. Markvicka, Y. Jin, C. Majidi, Soft-matter printed circuit board with UV laser micropatterning. *ACS Appl. Mater. Interfaces* **9**, 22055–22062 (2017).

33. M. G. Kim, H. Alrowais, S. Pavlidis, O. Brand, Size-scalable and high-density liquid-metal-based soft electronic passive components and circuits using soft lithography. *Adv. Funct. Mater.* **27**, 1604466 (2017).

34. T. Lu, L. Finkenauer, J. Wissman, C. Majidi, Rapid prototyping for soft-matter electronics. *Adv. Funct. Mater.* **24**, 3351–3356 (2014).

35. R. Guo, X. Sun, B. Yuan, H. Wang, J. Liu, Magnetic liquid metal (Fe-EGaIn) based multifunctional electronics for remote self-healing materials, degradable electronics, and thermal transfer printing. *Adv. Sci. (Weinh)* **6**, 1901478 (2019).

36. Y. Lin, O. Gordon, M. R. Khan, N. Vasquez, J. Genzer, M. D. Dickey, Vacuum filling of complex microchannels with liquid metal. *Lab Chip* **17**, 3043–3050 (2017).

37. A. Tabatabai, A. Fassler, C. Usiak, C. Majidi, Liquid-phase gallium-indium alloy electronics with microcontact printing. *Langmuir* **29**, 6194–6200 (2013).

38. K. Parida, G. Thangavel, G. Cai, X. Zhou, S. Park, J. Xiong, P. S. Lee, Extremely stretchable and self-healing conductor based on thermoplastic elastomer for all-three-dimensional printed triboelectric nanogenerator. *Nat. Commun.* **10**, 2158 (2019).

39. M.-G. Kim, D. K. Brown, O. Brand, Nanofabrication for all-soft and high-density electronic devices based on liquid metal. *Nat. Commun.* **11**, 1002 (2020).

40. Y. G. Park, H. S. An, J. Y. Kim, J. U. Park, High-resolution, reconfigurable printing of liquid metals with three-dimensional structures. *Sci. Adv.* **5**, eaaw2844 (2019).

41. L. Tang, J. Shang, X. Jiang, Multilayered electronic transfer tattoo that can enable the crease amplification effect. *Sci. Adv.* **7**, eabe3778 (2021).

42. L. Johnston, J. Yang, J. Han, K. Kalantar-Zadeh, J. Tang, Intermetallic wetting enabled high resolution liquid metal patterning for 3D and flexible electronics. *J. Mater. Chem. C* **10**, 921–931 (2022).

43. C. Laborde, F. Pittino, H. A. Verhoeven, S. G. Lemay, L. Selmi, M. A. Jongsma, F. P. Widdershoven, Real-time imaging of microparticles and living cells with CMOS nanocapacitor arrays. *Nat. Nanotechnol.* **10**, 791–795 (2015).

44. C.-H. Chiang, S. M. Won, A. L. Orsborn, K. J. Yu, M. Trumpis, B. Bent, C. Wang, Y. Xue, S. Min, V. Woods, C. Yu, B. H. Kim, S. B. Kim, R. Huq, J. Li, K. J. Seo, F. Vitale, A. Richardson, H. Fang, Y. Huang, K. Shepard, B. Pesaran, J. A. Rogers, J. Viventi, Development of a neural interface for high-definition, long-term recording in rodents and nonhuman primates. *Sci. Transl. Med.* **12**, eaay4682 (2020).

45. D. Khodagholy, J. N. Gelinas, T. Thesen, W. Doyle, O. Devinsky, G. G. Malliaras, G. Buzsáki, NeuroGrid: Recording action potentials from the surface of the brain. *Nat. Neurosci.* **18**, 310–315 (2015).

46. J. Viventi, D. H. Kim, L. Vigeland, E. S. Frechette, J. A. Blanco, Y. S. Kim, A. E. Avrin, V. R. Tiruvadi, S. W. Hwang, A. C. Vanleer, D. F. Wulsin, K. Davis, C. E. Gelber, L. Palmer, J. Van der Spiegel, J. Wu, J. Xiao, Y. Huang, D. Contreras, J. A. Rogers, B. Litt, Flexible, foldable, actively multiplexed, high-density electrode array for mapping brain activity in vivo. *Nat. Neurosci.* **14**, 1599–1605 (2011).

47. J. J. Jun, N. A. Steinmetz, J. H. Siegle, D. J. Denman, M. Bauza, B. Barbarits, A. K. Lee, C. A. Anastassiou, A. Andrei, Ç. Aydin, M. Barbic, T. J. Blanche, V. Bonin, J. Couto, B. Dutta, S. L. Gratiy, D. A. Gutnisky, M. Häusser, B. Karsh, P. Ledochowitsch, C. M. Lopez, C. Mitelut, S. Musa, M. Okun, M. Pachitariu, J. Putzeys, P. D. Rich, C. Rossant, W. L. Sun, K. Svoboda, M. Carandini, K. D. Harris, C. Koch, J. O'Keefe, T. D. Harris, Fully integrated silicon probes for high-density recording of neural activity. *Nature* **551**, 232–236 (2017).

48. T. Daeneke, K. Khoshmanesh, N. Mahmood, I. A. De Castro, D. Esrafilzadeh, S. J. Barrow, M. D. Dickey, K. Kalantar-Zadeh, Liquid metals: Fundamentals and applications in chemistry. *Chem. Soc. Rev.* **47**, 4073–4111 (2018).

49. A. Fassler, C. Majidi, Liquid-phase metal inclusions for a conductive polymer composite. *Adv. Mater.* **27**, 1928–1932 (2015).

50. S. Zhu, J. H. So, R. Mays, S. Desai, W. R. Barnes, B. Pourdeyhimi, M. D. Dickey, Ultrastretchable fibers with metallic conductivity using a liquid metal alloy core. *Adv. Funct. Mater.* **23**, 2308–2314 (2013).

51. E. J. Markvicka, M. D. Bartlett, X. Huang, C. Majidi, An autonomously electrically self-healing liquid metal-elastomer composite for robust soft-matter robotics and electronics. *Nat. Mater.* **17**, 618–624 (2018).

52. A. Leber, C. Dong, R. Chandran, T. Das Gupta, N. Bartolomei, F. Sorin, Soft and stretchable liquid metal transmission lines as distributed probes of multimodal deformations. *Nat. Electron.* **3**, 316–326 (2020).

53. J. Park, S. Wang, M. Li, C. Ahn, J. K. Hyun, D. S. Kim, D. K. Kim, J. A. Rogers, Y. Huang, S. Jeon, Three-dimensional nanonetworks for giant stretchability in dielectrics and conductors. *Nat. Commun.* **3**, 916 (2012).

54. S. Liu, D. S. Shah, R. Kramer-Bottiglio, Highly stretchable multilayer electronic circuits using biphasic gallium-indium. *Nat. Mater.* **20**, 851–858 (2021).

55. S. Veerapandian, W. Jang, J. B. Seol, H. Wang, M. Kong, K. Thiyagarajan, J. Kwak, G. Park, G. Lee, W. Suh, I. You, M. E. Kılıç, A. Giri, L. Beccai, A. Soon, U. Jeong, Hydrogen-doped viscoplastic liquid metal microparticles for stretchable printed metal lines. *Nat. Mater.* **20**, 533–540 (2021).

56. M. D. Dickey, R. C. Chiechi, R. J. Larsen, E. A. Weiss, D. A. Weitz, G. M. Whitesides, Eutectic gallium-indium (EGaln): A liquid metal alloy for the formation of stable structures in microchannels at room temperature. *Adv. Funct. Mater.* **18**, 1097–1104 (2008).

57. Y. L. Park, C. Majidi, R. Kramer, P. Brard, R. J. Wood, Hyperelastic pressure sensing with a liquid-embedded elastomer. *J. Micromech. Microeng.* **20**, 125029 (2010).

58. K. Nan, S. Babaee, W. W. Chan, J. L. P. Kuosmanen, V. R. Feig, Y. Luo, S. S. Srinivasan, C. M. Patterson, A. M. Jebran, G. Traverso, Low-cost gastrointestinal manometry via silicone–liquid-metal pressure transducers resembling a quipu. *Nat. Biomed. Eng.* **6**, 1092–1104 (2022).

59. J. Yan, Y. Lu, G. Chen, M. Yang, Z. Gu, Advances in liquid metals for biomedical applications. *Chem. Soc. Rev.* **47**, 2518–2533 (2018).

60. M. D. Dickey, Stretchable and soft electronics using liquid metals. *Adv. Mater.* **29**, 1606425 (2017).

61. K. J. Yu, D. Kuzum, S. W. Hwang, B. H. Kim, H. Juul, N. H. Kim, S. M. Won, K. Chiang, M. Trumpis, A. G. Richardson, H. Cheng, H. Fang, M. Thompson, H. Bink, D. Talos, K. J. Seo, H. N. Lee, S. K. Kang, J. H. Kim, J. Y. Lee, Y. Huang, F. E. Jensen, M. A. Dichter, T. H. Lucas, J. Viventi, B. Litt, J. A. Rogers, Bioresorbable silicon electronics for transient spatiotemporal mapping of electrical activity from the cerebral cortex. *Nat. Mater.* **15**, 782–791 (2016).

62. M. Park, J. Im, M. Shin, Y. Min, J. J. J. Park, H. Cho, S. Park, M. B. Shim, S. Jeon, D. Y. Chung, J. Bae, J. J. J. Park, U. Jeong, K. Kim, Highly stretchable electric circuits from a composite material of silver nanoparticles and elastomeric fibres. *Nat. Nanotechnol.* **7**, 803–809 (2012).

63. K. Molina-Luna, M. M. Buitrago, B. Hertler, M. Schubring, F. Haiss, W. Nisch, J. B. Schulz, A. R. Luft, Cortical stimulation mapping using epidurally implanted thin-film microelectrode arrays. *J. Neurosci. Methods* **161**, 118–125 (2007).

64. B. A. Hollenberg, C. D. Richards, R. Richards, D. F. Bahr, D. M. Rector, A MEMS fabricated flexible electrode array for recording surface field potentials. *J. Neurosci. Methods* **153**, 147–153 (2006).

65. J. Kim, J. A. Wilson, J. C. Williams, A cortical recording platform utilizing microECoG electrode arrays. *Annu. Int. Conf. IEEE Eng. Med. Biol. Soc.* **2007**, 5353–5357 (2007).

66. B. Rubehn, C. Bosman, R. Oostenveld, P. Fries, T. Stieglitz, A MEMS-based flexible multichannel ECoG-electrode array. *J. Neural Eng.* **6**, 036003 (2009).

67. P. Ledochowitsch, R. J. Félus, R. R. Gibboni, A. Miyakawa, S. Bao, M. M. Maharbiz, Fabrication and testing of a large area, high density, parylene MEMS μECoG array. *Proc. IEEE Int. Conf. Micro Electro Mech. Syst.*, 1031–1034 (2011).

68. J. Besle, C. A. Schevon, A. D. Mehta, P. Lakatos, R. R. Goodman, G. M. McKhann, R. G. Emerson, C. E. Schroeder, Tuning of the human neocortex to the temporal dynamics of attended events. *J. Neurosci.* **31**, 3176–3185 (2011).

69. M. A. Escabí, H. L. Read, J. Viventi, D. H. Kim, N. C. Higgins, D. A. Storace, A. S. K. Liu, A. M. Gifford, J. F. Burke, M. Campisi, Y. S. Kim, A. E. Avrin, J. Van der Spiegel, Y. Huang, M. Li, J. Wu, J. A. Rogers, B. Litt, Y. E. Cohen, A high-density, high-channel count, multiplexed μECOG array for auditory-cortex recordings. *J. Neurophysiol.* **112**, 1566–1583 (2014).

70. G. Hotson, D. P. McMullen, M. S. Fifer, M. S. Johannes, K. D. Katyal, M. P. Para, R. Armiger, W. S. Anderson, N. V. Thakor, B. A. Wester, N. E. Crone, Individual finger control of a modular prosthetic limb using high-density electrocorticography in a human subject. *J. Neural Eng.* **13**, 026017 (2016).

71. S. Kellis, L. Sorensen, F. Darvas, C. Sayres, K. O'Neill, R. B. Brown, P. House, J. Ojemann, B. Greger, Multi-scale analysis of neural activity in humans: Implications for micro-scale electrocorticography. *Clin. Neurophysiol.* **127**, 591–601 (2016).

72. D. Khodagholy, J. N. Gelinas, Z. Zhao, M. Yeh, M. Long, J. D. Greenlee, W. Doyle, O. Devinsky, G. Buzsáki, Organic electronics for high-resolution electrocorticography of the human brain. *Sci. Adv.* **2**, e1601027 (2016).

73. T. Kaiju, K. Doi, M. Yokota, K. Watanabe, M. Inoue, H. Ando, K. Takahashi, F. Yoshida, M. Hirata, T. Suzuki, High spatiotemporal resolution ECoG recording of somatosensory evoked potentials with flexible micro-electrode arrays. *Front. Neural Circuits.* **11**, 20 (2017).

74. B. A. Gozen, A. Tabatabai, O. B. Ozdoganlar, C. Majidi, High-density soft-matter electronics with micron-scale line width. *Adv. Mater.* **26**, 5211–5216 (2014).

75. M. G. Kim, C. Kim, H. Alrowais, O. Brand, Multiscale and uniform liquid metal thin-film patterning based on soft lithography for 3D heterogeneous integrated soft microsystems: Additive stamping and subtractive reverse stamping. *Adv. Mater. Technol.* **3**, 1800061 (2018).

76. S. H. Jeong, A. Hagman, K. Hjort, M. Jobs, J. Sundqvist, Z. Wu, Liquid alloy printing of microfluidic stretchable electronics. *Lab Chip* **12**, 4657–4664 (2012).

77. N. Lazarus, S. S. Bedair, I. M. Kierzewski, Ultrafine pitch stencil printing of liquid metal alloys. *ACS Appl. Mater. Interfaces* **9**, 1178–1182 (2017).

78. C. W. Park, Y. G. Moon, H. Seong, S. W. Jung, J. Y. Oh, B. S. Na, N. M. Park, S. S. Lee, S. G. Im, J. B. Koo, Photolithography-based patterning of liquid metal interconnects for monolithically integrated stretchable circuits. *ACS Appl. Mater. Interfaces* **8**, 15459–15465 (2016).

79. Y. Gao, H. Ota, E. W. Schaler, K. Chen, A. Zhao, W. Gao, H. M. Fahad, Y. Leng, A. Zheng, F. Xiong, C. Zhang, L. C. Tai, P. Zhao, R. S. Fearing, A. Javey, Wearable microfluidic diaphragm pressure sensor for health and tactile touch monitoring. *Adv. Mater.* **29**, 1701985 (2017).

80. J. W. Boley, E. L. White, G. T. C. Chiu, R. K. Kramer, Direct writing of gallium-indium alloy for stretchable electronics. *Adv. Funct. Mater.* **24**, 3501–3507 (2014).

81. C. Ladd, J. H. So, J. Muth, M. D. Dickey, 3D printing of free standing liquid metal microstructures. *Adv. Mater.* **25**, 5081–5085 (2013).

82. D. Kim, Y. Yoon, S. K. Kauh, J. Lee, Towards sub-microscale liquid metal patterns: Cascade phase change mediated pick-n-place transfer of liquid metals printed and stretched over a flexible substrate. *Adv. Funct. Mater.* **28**, 1800380 (2018).

83. C. Pan, K. Kumar, J. Li, E. J. Markvicka, P. R. Herman, C. Majidi, Visually imperceptible liquid-metal circuits for transparent, stretchable electronics with direct laser writing. *Adv. Mater.* **30**, 1706937 (2018).

84. M. R. Khan, J. Bell, M. D. Dickey, Localized instabilities of liquid metal films via in-plane recapillarity. *Adv. Mater. Interfaces* **3**, 1600546 (2016).

85. E. Bihar, T. Roberts, M. Saadaoui, T. Hervé, J. B. De Graaf, G. G. Malliaras, Inkjet-printed PEDOT:PSS electrodes on paper for electrocardiography. *Adv. Healthc. Mater.* **6**, 1601167 (2017).

86. A. Albrecht, A. Rivadeneyra, A. Abdellah, P. Lugli, J. F. Salmerón, Inkjet printing and photonic sintering of silver and copper oxide nanoparticles for ultra-low-cost conductive patterns. *J. Mater. Chem. C* **4**, 3546–3554 (2016).

87. M. Tavakoli, M. H. Malakooti, H. Paisana, Y. Ohm, D. Green Marques, P. Alhais Lopes, A. P. Piedade, A. T. de Almeida, C. Majidi, EGaIn-assisted room-temperature sintering of silver nanoparticles for stretchable, inkjet-printed, thin-film electronics. *Adv. Mater.* **30**, 1801852 (2018).

88. S. H. Ke, Q. W. Xue, C. Y. Pang, P. W. Guo, W. J. Yao, H. P. Zhu, W. Wu, Printing the ultra-long ag nanowires inks onto the flexible textile substrate for stretchable electronics. *Nanomaterials (Basel)* **9**, 686 (2019).

89. Y. Liang, Y. Zhao, Z. Cheng, Y. Deng, Y. Xiao, H. Cheng, P. Zhang, Y. Huang, H. Shao, L. Qu, Electric power generation via asymmetric moisturizing of graphene oxide for flexible, printable and portable electronics. *Energ. Environ. Sci.* **11**, 1730–1735 (2018).

90. T. Lim, H. J. Kim, H. Zhang, S. Lee, Screen-printed conductive pattern on spandex for stretchable electronic textiles. *Smart Mater. Struct.* **30**, 075006 (2021).

91. A. Dallinger, K. Keller, H. Fitzek, F. Greco, Stretchable and skin-conformable conductors based on polyurethane/laser-induced graphene. *ACS Appl. Mater. Interfaces* **12**, 19855–19865 (2020).

92. M. Zhang, J. J. Sun, M. Khatib, Z. Y. Lin, Z. H. Chen, W. Saliba, A. Gharra, Y. D. Horev, V. Kloper, Y. Milyutin, T. P. Huynh, S. Brandon, G. Shi, H. Haick, Time-space-resolved origami hierarchical electronics for ultrasensitive detection of physical and chemical stimuli. *Nat. Commun.* **10**, 1120 (2019).

93. E. Quain, T. S. Mathis, N. Kurra, K. Maleski, K. L. Van Aken, M. Alhabeb, H. N. Alshareef, Y. Gogotsi, Direct writing of additive-free MXene-in-water ink for electronics and energy storage. *Adv. Mater. Technol.* **4**, 1800256 (2019).

94. K. Shrivas, A. Ghosale, T. Kant, P. K. Bajpai, R. Shankar, The direct-writing of low cost paper based flexible electrodes and touch pad devices using silver nano-ink and ZnO nanoparticles. *RSC Adv.* **9**, 17868–17876 (2019).

95. Y. Zhang, L. Zhang, K. Cui, S. Ge, X. Cheng, M. Yan, J. Yu, H. Liu, Flexible electronics based on micro/nanostructured paper. *Adv. Mater.* **30**, e1801588 (2018).

96. Y. Wang, J. Wang, S. Cao, D. Kong, A stretchable and breathable form of epidermal device based on elastomeric nanofibre textiles and silver nanowires. *J. Mater. Chem. C* **7**, 9748–9755 (2019).

97. Q. Zhang, Y. Gao, J. Liu, Atomized spraying of liquid metal droplets on desired substrate surfaces as a generalized way for ubiquitous printed electronics. *Appl. Phys. A.* **116**, 1091–1097 (2014).

98. C. Wang, M. Zhang, K. Xia, X. Gong, H. Wang, Z. Yin, B. Guan, Y. Zhang, Intrinsically stretchable and conductive textile by a scalable process for elastic wearable electronics. *ACS Appl. Mater. Interfaces* **9**, 13331–13338 (2017).

99. I. Wicaksono, C. I. Tucker, T. Sun, C. A. Guerrero, C. Liu, W. M. Woo, E. J. Pence, C. Dagdeviren, A tailored, electronic textile conformable suit for large-scale spatiotemporal physiological sensing in vivo. *npj Flex. Electron.* **4**, 5 (2020).

100. M. J. Yun, Y. H. Sim, D. Y. Lee, S. I. Cha, Highly stretchable large area woven, knitted and robust braided textile based interconnection for stretchable electronics. *Sci. Rep.* **11**, 4038 (2021).

Science Advances

Wafer-patterned, permeable, and stretchable liquid metal microelectrodes for implantable bioelectronics with chronic biocompatibility

Qiuna Zhuang, Kuanming Yao, Mengge Wu, Zhuogui Lei, Fan Chen, Jiyu Li, Quanjing Mei, Yingying Zhou, Qiyao Huang, Xin Zhao, Ying Li, Xinge Yu, and Zijian Zheng

View the article online
https://www.science.org/doi/10.1126/sciadv.adg8602
Permissions
https://www.science.org/help/reprints-and-permissions